in the northern hemisphere are as strong as the regions in the south.

In addition to explaining the occurrence of a strong field in only one hemisphere, our model is also able to explain the conflicts between various Mars paleomagnetic studies and rotational stability studies. The inferred paleomagnetic pole positions vary in location depending on the individual crustal anomaly used (*25*, *26*). Some of the paleopoles are also located in equatorial regions near the Tharsis bulge and hence are far from the current geographic poles. This has been interpreted as evidence for a large true polar wander event that relocated Tharsis from polar to equatorial regions in early Mars history (*27*). However, large Tharsis-driven true polar wander is in conflict with rotational stability studies (*28*, *29*) that demonstrate that the present-day gravitational figure of Mars favors a small Tharsis-driven true-polar wander scenario.

An assumption made in the paleomagnetic studies is that the dynamo-generated magnetic field was axial-dipolar dominated. This assumption implies that the magnetic pole coincided with the rotation pole and is used extensively in Earth paleomagnetic studies. Our models would dictate that the Mars dynamo-generated field was not axial-dipolar dominated and hence that the magnetic poles would not coincide with the rotation poles, rendering paleopole interpretations useless. In addition, because our dynamo-generated fields are multipolar, individual crustal magnetic fields at different locations can point to different paleomagnetic poles, thereby explaining the discrepancies in the different paleomagnetic studies.

A single-hemisphere dynamo also has implications for evolution of the martian atmosphere. A strong dynamo-generated magnetic field can more easily explain the intense crustal magnetism. However, efficient atmospheric erosion, necessary to explain the loss of Mars' early thick atmosphere, favors a weak internal magnetic field (*30*). Our single-hemisphere dynamo may provide an elegant solution to this problem because the northern hemisphere would be prone to atmospheric removal early in solar system history when the young Sun was more active (*31*), but the southern hemisphere could still possess a strong magnetic field in which the crustal rocks could magnetize.

### References and Notes


1. M. H. Acuna *et al*., *Science* **284**, 790 (1999).
2. B. Langlais, M. E. Purucker, M. Mandea, *J. Geophys. Res.* **109**, E02008 (2004).
3. B. P. Weiss *et al*., *Earth Planet. Sci. Lett.* **201**, 449 (2002).
4. L. A. Edgar, H. V. Frey, *Geophys. Res. Lett.* **35**, L02201 (2008).
5. M. T. Zuber *et al*., *Science* **287**, 1788 (2000).
6. S. C. Solomon *et al*., *Science* **307**, 1214 (2005) and references therein.
7. H. V. Frey, *J. Geophys. Res.* **111**, E08S91 (2006).
8. S. Zhong, M. T. Zuber, *Earth Planet. Sci. Lett.* **189**, 75 (2001).
9. J. H. Roberts, S. Zhong, *J. Geophys. Res.* **111**, E06013 (2006).
10. L. T. Elkins-Tanton, E. M. Parmentier, P. C. Hess, *Meteorit. Planet. Sci.* **38**, 1753 (2003).
11. L. T. Elkins-Tanton, S. E. Zaranek, E. M. Parmentier, P. C. Hess, *Earth Planet. Sci. Lett.* **236**, 1 (2005).
12. Y. Ke, V. S. Solomatov, *J. Geophys. Res.* **111**, E10001 (2006).
13. D. E. Wilhelms, S. W. Squyres, *Nature* **309**, 138 (1984).
14. H. Frey, R. A. Shultz, *Geophys. Res. Lett.* **15**, 229 (1988).
15. F. Nimmo, M. S. Gilmore, *J. Geophys. Res.* **106**, 12315 (2001).
16. T. R. Watters, P. J. McGovern, R. P. Irwin III, *Annu. Rev. Earth Planet. Sci.* **35**, 621 (2007).
17. J. C. Andrews-Hanna, M. T. Zuber, W. B. Banerdt, *Nature* **453**, 1212 (2008).
18. W. A. Watters, M. T. Zuber, B. H. Hager, *J. Geophys. Res.*, in press.
19. W. Kuang, J. Bloxham, *Nature* **389**, 371 (1997).
20. W. Kuang, J. Bloxham, *J. Comput. Phys.* **153**, 51 (1999).
21. Additional information on the numerical methods is available as supporting material on *Science* Online.
22. E. Grote, F. H. Busse, *Phys. Rev. E* **62**, 4457 (2000).
23. G. A. Glatzmaier, R. S. Coe, L. Hongre, P. H. Roberts, *Nature* **401**, 885 (1999).
24. M. Kono, P. H. Roberts, *Rev. Geophys.* **40**, 1013 (2002).
25. Y. Quesnel, B. Langlais, C. Sotin, *Planet. Space Sci.* **55**, 258 (2007), and references therein.
26. B. Langlais, M. Purucker, *Planet. Space Sci.* **55**, 270 (2007); and references therein.
27. K. F. Sprenke, L. L. Baker, A. F. Williams, *Icarus* **174**, 486 (2005); and references therein.
28. A. Daradich *et al*., *Icarus* **194**, 463 (2008).
29. J. T. Perron, J. X. Mitrovica, M. Manga, I. Matsuyama, M. A. Richards, *Nature* **447**, 840 (2007).
30. V. Dehant *et al*., *Space Sci. Rev.* **129**, 279 (2007).
31. Y. N. Kulikov *et al*., *Space Sci. Rev.* **129**, 207 (2007).


32. S.S. is partially funded by the National Science and Engineering Research Council (NSERC) of Canada. The numerical simulations in this study were performed on supercomputing resources partially funded by the Canadian Foundation for Innovation (CFI) and the Ontario Research Fund (ORF).


### Supporting Online Material

www.sciencemag.org/cgi/content/full/321/5897/1822/DC1
Materials and Methods
SOM Text
Figs. S1 and S2

29 May 2008; accepted 19 August 2008
10.1126/science.1161119

# The Structure and Dynamics of Mid-Ocean Ridge Hydrothermal Systems

**D. Coumou,* T. Driesner, C. A. Heinrich**

**Sub-seafloor hydrothermal convection at mid-ocean ridges transfers 25% of the Earth's heat flux and can form massive sulfide ore deposits. Their three-dimensional (3D) structure and transient dynamics are uncertain. Using 3D numerical simulations, we demonstrated that convection cells self-organize into pipelike upflow zones surrounded by narrow zones of focused and relatively warm downflow. This configuration ensures optimal heat transfer and efficient metal leaching for ore-deposit formation. Simulated fluid-residence times are as short as 3 years. The concentric flow geometry results from nonlinearities in fluid properties, and this may influence the behavior of other fluid-flow systems in Earth's crust.**

Hydrothermal convection at mid-ocean ridge spreading centers transports a major part of Earth's total heat flux, substantially affects the chemistry of crust and overlying ocean, and provides nutrients for chemosynthetic life on and beneath the sea floor. Mass, heat, and associated chemical fluxes from the crust to the ocean at mid-ocean ridge spreading centers are large (*1*, *2*). Fundamental features of this flow, such as the location of seawater recharge and the relative importance of off- versus along-axis convection, are still uncertain. Recent studies of active (*3*) and ancient (*4*) systems show that discharge can be highly focused in pipelike regions, possibly continuing to the base of the hydrothermal system (*3*). Recharge is often thought to occur over extensive areas (*5*, *6*), with off-axis faults guiding fluid pathways toward the base of the hydrothermal system. A common alternative view is that of fluid circulation being restricted to a high-permeability along-axis zone (*7*, *8*). Micro-earthquake data indicate that recharge can be focused close to the spreading center in some systems (*9*).

Recent two-dimensional (2D) numerical studies that included accurate thermodynamic properties of water have shown that the nonlinear dependence of fluid properties on pressure and temperature is a first-order control, determining the self-organization of convection cells (*10*–*12*). Quantitative 3D numerical models have been applied to low-permeability (*13*) or sedimented systems (*14*) and to a configuration with an along-axis high-permeability fracture (*15*, *16*) but not to the more highly permeable basaltic systems, which represent the greater and most active part of mid-ocean ridge spreading centers. Here, we describe a 3D model that represents the hydrothermal system without geological complexity so as to identify the first-order physical factors controlling the behavior of mid-ocean ridge convection cells.

The governing equations are an appropriate version of Darcy's law (*17*), conservation of mass and energy in an incompressible porous medium (*12*) and an accurate equation of state for pure water (*18*). Using pure water substantially reduces the computational complexity because pure water above the critical pressure (21.1 MPa) is always a single-phase fluid with properties closely resembling those of seawater. Two-dimensional across-axis simulations including the full-phase

Department of Earth Sciences, Eidgenössische Technische Hochschule–Zurich, Clausiusstrasse 25, Zurich 9082, Switzerland.

*To whom correspondence should be addressed. E-mail: coumou@pik-potsdam.de

relations of seawater have shown that the overall narrow shape of the upwelling plume remains similar in spite of phase separation (*19*), hence the simplification employed here is justified. The equations are solved within the 3D box shown in Fig. 1, which has been discretized by a total of ~2.5 million tetrahedral elements. The total amount of energy added to the system can be estimated from the spreading rate of the oceanic plates. Magma crystallization and cooling to ambient temperatures release energy up to ~120 MW/km of the spreading axis (*2*). Direct measurements from individual vent fields or ridge segments have given substantially larger values, indicating that magma supply is episodic and local (*20*–*22*). In the model, we set the heat flux at an intermediate value of 350 MW/km, which is distributed along the bottom in a Gaussian profile that mimics an elongated magma chamber with an across-axial width of roughly 1 km (Fig. 1) (*23*). We set a bulk permeability of $k = 5.0 \times 10^{-14}$ m$^2$. At these specific values of permeability and heat flux, the temperature near the bottom of the model establishes itself to be close to the expected magmatic temperatures of ~1200°C (*24*). At lower permeability, the system cannot remove heat fast enough, and the system heats up unrealistically. At higher permeabilities, heat is mined faster, suppressing bottom boundary temperatures to values much smaller than magmatic temperatures. The top boundary represents the sea floor and is kept at a pressure of 25 MPa, representing an ocean depth of roughly 2.5 km. To allow hot fluids to vent through the top, we used a mixed thermal boundary condition (*11*, *12*): In elements experiencing upflow, the thermal gradient is set to zero to represent unobstructed outflow to the ocean, whereas elements experiencing downflow take in 10°C water.

In the simulations, after a short initialization period, convection developed into pipelike upflow regions, spaced at regular distances of roughly 500 m (Fig. 2A). Although thermal instabilities periodically form and rise close to the axial center, the locations of the main upflow regions remain relatively fixed. Within these pipes, fluids of ~400°C move upward vigorously and vent at the sea floor, forming near-circular discharge areas. The surface area of these fields is ~$2 \times 10^4$ m$^2$, which is in good agreement with the range observed for natural black smoker fields of $3 \times 10^3$ m$^2$ to $1 \times 10^5$ m$^2$ (*25*). Most of the downflow happens in concentric tube-shaped regions directly surrounding the upflow plumes (Fig. 2, A to C). Fluid temperatures in these regions ranged from 100° to 300°C at already shallow depth. At a radius of less than twice that of the upflow zone, the downward mass flux reached a value five times as large as the average downward mass flux and about half the maximum upward flux. At a depth of 500 m, the integrated upward mass flux through the whole model is ~800 kg/s, which implies ~200 kg/s per kilometer of ridge segment and ~100 kg/s per vent field. Roughly two-thirds of this mass is provided by downflow in the warm near-axial regions. Elevated temperatures of the downflowing fluids reaching 300°C imply that substantial heat is recirculated; roughly one-quarter of the heat traveling upward is lost conductively to the adjacent downflow zones, in which it is recirculated back to the bottom. This recirculation process therefore controls the thermal structure of the downflow zone, heating it to average temperatures of ~200°C. Relatively warm downflow has been observed in 2D models (*26*), in which downflow has to take place in between

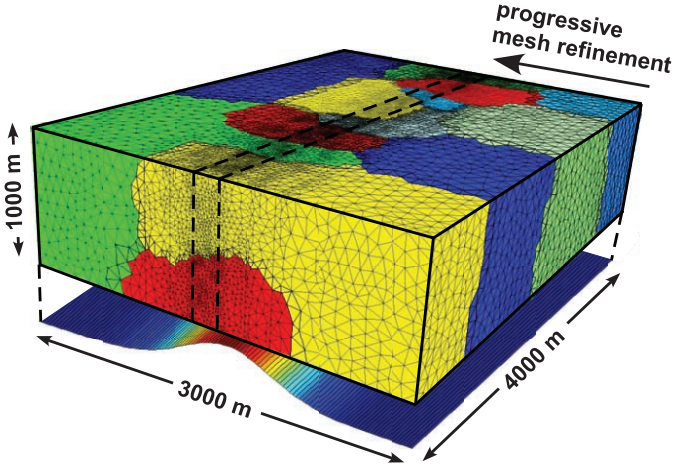


**Fig. 1.** 3D mesh consisting of 2.5-m tetrahedron elements. Resolution is refined toward the axial center, with the finest resolution between the dashed lines, and colors indicate computational domains assigned to separate processors (*23*). At the bottom boundary, the bell-shaped form of the heat flux profile is plotted, ranging from 10 W/m$^2$ (blue) to 300 W/m$^2$ (red).

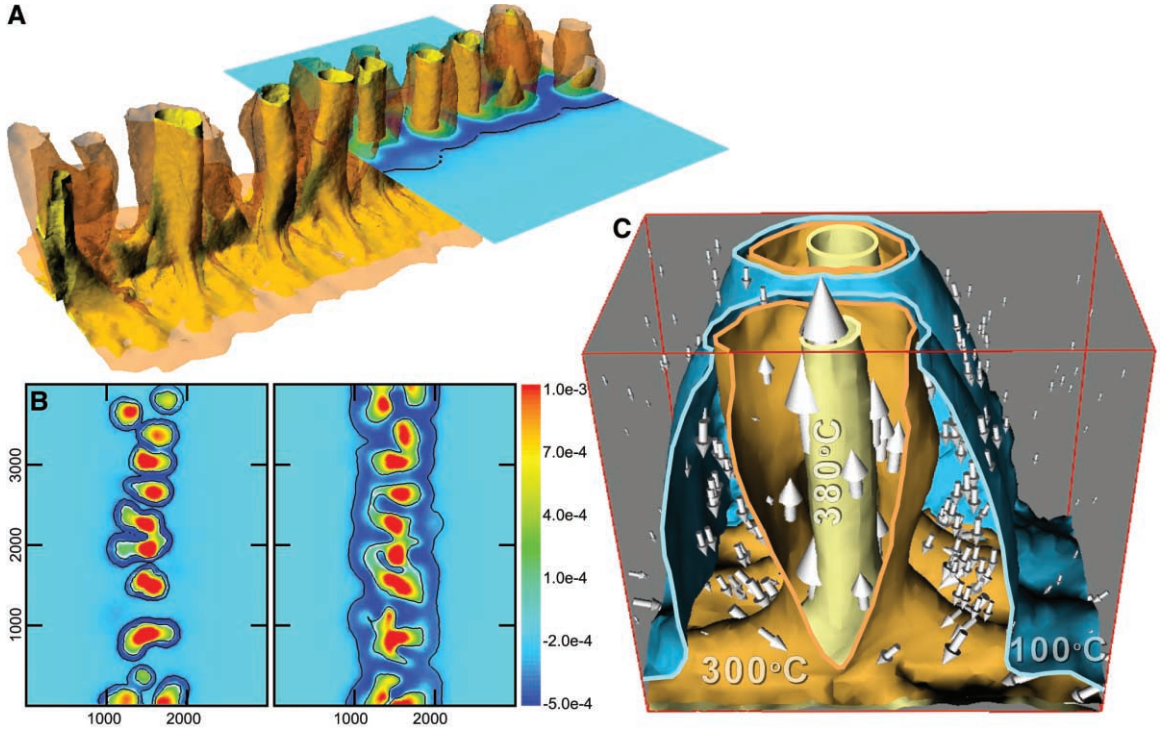


**Fig. 2.** Thermal and fluid-flow structure of the simulation after ~100 years. (**A**) The 3D contours of the 300°C (transparent) and 380°C (yellow) isotherms. The horizontal cross-section plots vertical mass fluxes [scale as plotted in (B)]. (**B**) Mass fluxes in kilograms per square meter per second through horizontal cross-sections at 100- and 500-m depth. Thin black lines plot the 100°C and 300°C isotherms, and the white line separates the upflowing from downflowing regions (*x* axis, meters; *y* axis, meters). (**C**) Cross-section through a thermal plume plotting 100°C (blue), 300°C (brown), and 380°C (yellow) isotherms as well as mass fluxes (arrows). High-hydraulic-conductivity downflow zones between the 100° and 300°C isotherms are clearly visible.

hot upflow zones, but is not naturally expected in 3D. Darcy fluxes in the system are ~$5.0 \times 10^{-6}$ m/s in the upflow zone and ~$0.75 \times 10^{-6}$ m/s in the surrounding near-axial downflow zone. By converting these values to actual pore velocities, a residence time of only ~3 years is calculated for a fluid particle entering the system through the proximal recharge zone, traveling to the base of the hydrothermal cell, and flowing out again through the black smoker. This short travel time is in agreement with recent estimates made with natural radionuclide tracers (*27*, *28*).

To understand why this system evolves this way, we analyzed the steady-state pressure gradient ($\partial p/\partial z$) in a simplified geometry, taking account of the nonlinearity of the fluid properties. In the near-axial region, the vertical pressure gradient must have a value between that of a cold and hot hydrostatic, so that cold fluids can be brought downward and hot fluids can be brought upward. As a first approximation, we assumed that recharge is limited to a region directly surrounding a pipe-shaped upflow zone (fig. S1). The mass balance between up- and downflowing water is

$$A_u \rho_u \frac{k_u}{\mu_u}\left[\frac{\partial p}{\partial z} - \rho_u g\right] = A_d \rho_d \frac{k_d}{\mu_d}\left[\rho_d g - \frac{\partial p}{\partial z}\right] \quad (1)$$

Here, $A_u$ is the cross-sectional area of the upflow zone and $A_d$ is the cross-sectional area of the downflow zone. Subscripts u and d indicate properties of the upwelling and the downwelling fluid, respectively; $\rho$ is the water density; $\mu$ is the water viscosity; and $g$ is the acceleration due to gravity (fig. S1). Equation 1 assumes that horizontal pressure gradients between up- and downflow areas can be neglected. This assumption is allowed in the near-axial region because there the fluid flow is dominantly vertical. The vertical pressure gradient can be expressed in terms of the density $\rho_n$ of a fictitious neutrally buoyant fluid, according to $\partial p/\partial z = \rho_n g$. Equation 1 can now be written as

$$\frac{\rho_n - \rho_u}{\rho_d - \rho_u} = \frac{1}{1 + \gamma R} \quad (2)$$

Here, the geometric constant $\gamma$ represents the ratio $A_u k_u / A_d k_d$ and $R$ is the ratio of fluid properties $\mu_d \rho_u / \mu_u \rho_d$. Physically, the product $\gamma R$ can be seen as the ratio of the resistance against flow in the downflow region over that in the upflow region and, depending on pressure and temperature, can have values ranging from 0.1 to 10 $\gamma$. From Eq. 2, we can derive an expression for the fluxibility $F$, defined as the ability of a system to transport energy by buoyancy-driven convection

$$F = \frac{\rho_u (h_u - h_d)(\rho_d - \rho_u)}{\mu_u} \frac{1}{1 + \gamma R} \quad (3)$$

where $h$ is the specific enthalpy of the fluid. Equation 3 is an extension of the ordinary definition of fluxibility (*29*) because it allows resistance in the downwelling limb as well as the upwelling limb. In the limit $\gamma \to 0$, in which the resistance of the downwelling limb is negligible as compared with that of the upwelling limb, Eq. 3 reduces to the original definition of fluxibility (*29*, *30*).

Heating water from 10° to 200°C decreases $\mu$ by approximately one order of magnitude, whereas $\rho$ changes by only about 10% (Fig. 3A). As a consequence, 200°C fluids can be brought downward highly efficiently: The greatly reduced viscosity makes them mobile, whereas their only weakly decreased density maintains a substantial downward buoyancy force as compared with the upflow zone. Heating the fluid to even higher temperatures would cause the density to decrease substantially and hence lower the downward buoyancy force. Downward mass transport can therefore be optimized at temperatures of around 200°C.

In order to analyze our numerical results, we took $\gamma$ as ~1 because $k$ is homogeneous ($k_d = k_u$), and the area of upflow is roughly the same as the area of increased downflow (Fig. 2B). Figure 3B plots $F$ against temperatures of the up- and downflowing fluid using $\gamma = 1$. It shows that energy transport can be maximized when upflowing water reaches temperatures of ~400°C and downflowing water is ~200°C, exactly like the thermal structure observed in the numerical simulations. The thermal structure of the numerical simulations featured enhanced downflow for fluids in the temperature range from 100° to 300°C, which fits with the peak of maximum fluxibility in Fig. 3B. At these conditions, a neutrally buoyant fluid has a density of ~600 kg/m$^3$ (Fig. 3C), implying that $\partial p/\partial z$ is ~6000 Pa/m, which is in agreement with simulation results. If upflowing fluids have either a lower or higher temperature than ~400°C, then their hydraulic resistance will increase, hence the pressure gradient has to increase to drive such fluids upwards, resulting in larger neutral buoyancies (Fig. 3C). Similarly, the resistance of the downflow zone increases if its temperature is either larger or smaller than ~200°C. Cooling a ~200°C fluid will increase its viscosity more rapidly than its density, whereas heating a ~200°C fluid will decrease its density faster than its viscosity (see Fig. 3A). Both effects result in a larger hydraulic resistance of the fluid. This analysis shows that the convection cells operate in a state of least hydraulic resistance in order to maximize the overall efficiency of energy transport. Thus, surprisingly, substantial recirculation of heat unexpectedly enhances mass fluxes through the system and thereby increases the overall heat transport of the cell. Previous studies indicated that black smoker systems could well be operating in a state of maximum energy transport (*30*–*33*), explaining why black smoker vent fields are often close to but never higher than ~400°C (*11*).

Convection cells evolve toward and remain in this state of least resistance by counteracting feedback mechanisms that self-regulate the flow in convection cells. For instance, increasing resistance by cooling the downflow zone to temperatures lower than ~200°C slows down the fluid flow through the system. This reduced flow increases conductive heat losses from the upflow area, heating up the downflow area again to temperatures of ~200°C. Furthermore, the upflow temperature cannot become hotter than ~400°C (*11*). Therefore, if convection stagnates because of external forces, the boundary layer between the magma chamber and hydrothermal cell will broaden, but upflow temperatures will stay at ~400°C.

The regular spacing between black smoker fields has previously been explained with a slot-convection model, in which convection dominantly takes place in a high-permeability axial plane and therefore could be considered a 2D system (*12*). Our simulations show that this restriction is not required and that, at high heat-flux conditions, convection naturally forms individual black smoker fields at regular spacing because of the nonlinear temperature and pressure dependence of the fluid's properties.

The Main Endeavour Field (MEF) on the Juan de Fuca ridge appears to be a natural exam-

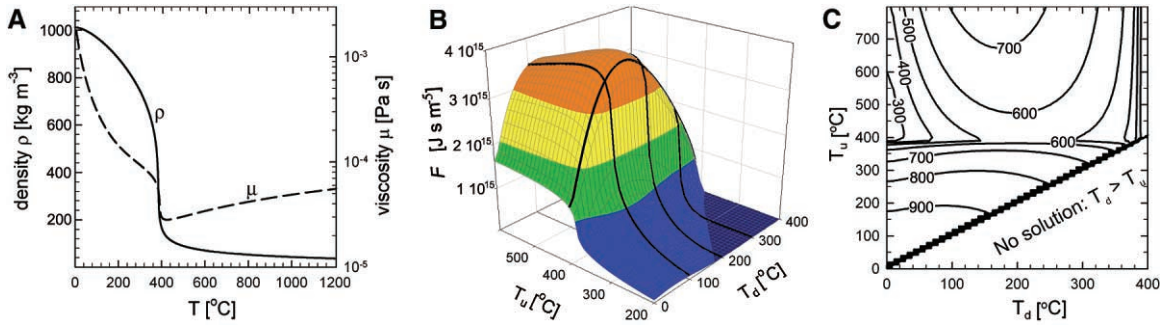


**Fig. 3.** (**A**) Density (solid) and viscosity (dashed) as a function of temperature at 30 MPa. (**B**) $F$ plotted against upwelling and downwelling temperatures (Eq. 3). Solid black lines follow contours at downwelling temperature ($T_d$) = 100°C, $T_d$ = 200°C, $T_d$ = 300°C, and $T_u$ = 400°C. Blue, 0 < F < 1e15; Green, 1e15 < F < 2e15; Yellow, 2e15 < F < 3e15; and Orange, 3e15 < F < 4e15. (**C**) Neutral density (in kilograms per cubic meter) plotted against upwelling and downwelling temperatures.

ple closely matching our simulation results. There, regularly spaced vent sites, with black smokers venting fluids close to 400°C, have been active for several years (*34*, *35*). Magnetic anomaly data show that upflow zones are narrow pipelike structures that reach to a depth of at least a few hundreds of meters and possibly to the base of the hydrothermal system with a regular spacing comparable with that in our simulations (*3*). Though natural systems are geologically much more complex than the numerical model described here, we suggest that the MEF is likely to operate in a state of maximum energy transport, with recharge occurring close to the vent sites. The optimal site for future in situ tracer injection experiments would therefore be about twice the radius of a black smoker vent field. The relatively short residence times resulting from our calculations also indicate that such an experiment can lead to a successful tracer test within a realistic time frame.

Massive sulfide ore deposits form when convecting seawater leaches metals from new basaltic crust and reprecipitates them as sulfides at the outflow points of active black smokers. The solubility of iron, zinc, and copper increases almost exponentially with temperature (*36*). Our simulations indicate that the average temperature of fluid-rock interaction is much higher than would be expected from dispersed seawater infiltration across the spreading axis (*37*). As a result, solubility-limited leaching is expected to be much more effective by including large parts of the hot downflow path and not being restricted to the basal reaction zone of the system. With an average copper content in mid-ocean ridge basalt of 25 parts per million, a typical small seafloor sulfide deposit of 0.2 million metric tons containing 3% copper (*38*) can be formed by leaching only the upflow zone and its immediately surrounding hot downflow zone. The copper solubility in this region varies from ~$10^{-7}$ mol/kg at 200°C to ~$10^{-4}$ mol/kg at 350°C, ensuring that the metals are quickly leached and a deposit can form within a period of 100 to 1000 years.

### References and Notes


1. C. Stein, S. Stein, *J. Geophys. Res.* **99**, 3081 (1994).
2. A. Fisher, in *Energy and Mass Transfer in Marine Hydrothermal Systems*, P. E. Halbach, V. Tunnicliffe, J. R. Hein, Eds. (Dahlem Univ. Press, Berlin, 2003), vol. 89, pp. 29–52.
3. M. Tivey, H. Johnson, *Geology* **30**, 979 (2002).
4. L. Coogan *et al.*, *Am. J. Sci.* **306**, 389 (2006).
5. H. Johnson, K. Becker, R. Von Herzen, *Geophys. Res. Lett.* **20**, 1875 (1993).
6. S. Kelley, J. Baross, J. Delaney, *Annu. Rev. Earth Planet. Sci.* **30**, 385 (2002).
7. P. Nehlig, T. Juteau, *Mar. Geol.* **84**, 209 (1988).
8. W. Wilcock, A. Fisher, *Geophys. Monogr.* **144**, 51 (2004).
9. M. Tolstoy, F. Waldhause, D. Bohnenstiehl, R. Weekly, W. Kim, *Nature* **451**, 181 (2008).
10. S. Ingebritsen, D. O. Hayba, *Geophys. Res. Lett.* **21**, 2199 (1994).
11. T. Jupp, A. Schultz, *Nature* **403**, 880 (2000).
12. D. Coumou, T. Driesner, S. Geiger, C. Heinrich, S. Matthai, *Earth Planet. Sci. Lett.* **245**, 218 (2006).
13. B. Travis, D. Janecky, N. Rosenberg, *Geophys. Res. Lett.* **18**, 1441 (1991).
14. M. Rabinowicz, J. Boulegue, P. Genthon, *J. Geophys. Res.* **103**, 24045 (1998).
15. M. Rabinowicz, J. Sempéré, P. Genthon, *J. Geophys. Res.* **104**, 29275 (1999).
16. F. Fontaine, M. Rabinowicz, J. Boulegue, *Earth Planet. Sci. Lett.* **184**, 407 (2001).
17. S. Ingebritsen, W. Sanford, C. Neuzil, *Groundwater in Geologic Processes* (Cambridge Univ. Press, Cambridge, ed. 2, 2006).
18. G. Haar, Kell, *NBS/NRC Steam Tables* (Hemisphere Publishing, New York, 1984).
19. D. Coumou, thesis, Eidgenössische Technische Hochschule–Zurich, Switzerland (2008).
20. U. Ginster, M. Mottl, R. Von Herzen, *J. Geophys. Res.* **99**, 4937 (1994).
21. E. Baker, T. Urabe, *J. Geophys. Res.* **101**, 8685 (1996).
22. P. Ramondenc, L. Germanovich, K. Von Damm, R. Lowell, *Earth Planet. Sci. Lett.* **245**, 487 (2006).
23. Materials and methods are available as supporting material on *Science* Online.
24. J. Sinton, R. Detrick, *J. Geophys. Res.* **97**, 197 (1992).
25. R. Lowell, A. Rona, R. Von Herzen, *J. Geophys. Res.* **100**, 327 (1995).
26. F. Fontaine, W. Wilcock, *Geochem. Geophys. Geosyst.* **8**, Q07010 (2007).
27. D. Kadko, D. Butterfield, *Geochim. Cosmochim. Acta* **62**, 1521 (1998).
28. D. Kadko, G. K., D. Butterfield. *Geochim. Cosmochim. Acta* **71**, 6019 (2007).
29. C. Lister, *Geophys. J. Int.* **120**, 45 (1995).
30. T. Jupp, A. Schultz, *J. Geophys. Res.* **109**, 10.1029/2003JB002697 (2004).
31. W. Malkus, *Proc. R. Soc. London. Ser. A* **225**, 196 (1954).
32. F. Busse, D. Joseph, *J. Fluid Mech.* **54**, 521 (1972).
33. W. S. D. Wilcock, *J. Geophys. Res.* **103**, 2585 (1998).
34. E. M. Van Ark *et al.*, *J. Geophys. Res.* **112**, 10.1029/2005JB004210 (2007).
35. D. Glickson, D. Kelley, J. Delaney, *Geochem. Geophys. Geosyst.* **8**, Q06010 (2007).
36. J. Hemley, G. Cygan, J. Fein, G. Robinson, W. Angelo, *Econ. Geol.* **87**, 1 (1992).
37. J. Franklin, H. Gibson, I. Jonasson, A. Galley, in *Economic Geology, 100th Anniversary Volume*, J. W. Hedenquist, J. F. H. Thompson, R. J. Goldfarb, J. P. Richards, Eds. (Society of Economic Geologists, Littleton, CO, 2005), pp. 523–560.
38. M. Hannington, I. Jonasson, P. Herzig, S. Petersen, *Geophys. Monogr.* **91**, 115 (1995).


39. This work was supported by the Swiss National Science Foundation (grant 200020-107955). The authors thank S. Geiger for providing the mesh depicted in Fig. 1 and S. Ingebritsen, P. Weiss, L. Cathles, and three anonymous reviewers for useful discussions as well as careful proofreading of earlier versions of the manuscript.


### Supporting Online Material

www.sciencemag.org/cgi/content/full/321/5897/1825/DC1
Materials and Methods
Fig. S1
References

24 April 2008; accepted 28 July 2008
10.1126/science.1159582

# Neodymium-142 Evidence for Hadean Mafic Crust

**Jonathan O'Neil,[1]* Richard W. Carlson,[2] Don Francis,[1] Ross K. Stevenson[3]**

**Neodymium-142 data for rocks from the Nuvvuagittuq greenstone belt in northern Quebec, Canada, show that some rock types have lower $^{142}Nd/^{144}Nd$ ratios than the terrestrial standard ($\varepsilon^{142}Nd = -0.07$ to $-0.15$). Within a mafic amphibolite unit, $^{142}Nd/^{144}Nd$ ratios correlate positively with Sm/Nd ratios and produce a $^{146}Sm$-$^{142}Nd$ isochron with an age of $4280^{+53}_{-81}$ million years. These rocks thus sample incompatible-element-enriched material formed shortly after Earth formation and may represent the oldest preserved crustal section on Earth.**

The past decade has seen dramatic discoveries concerning the oldest rocks on Earth, with precise zircon ages pushing the terrestrial rock record back beyond 4 billion years ago (Ga) (*1*) and the detrital zircon record to beyond 4.3 Ga (*2*). Because zircon is a rare to nonexistent phase in most mafic rocks, prospecting for ancient crust through zircon analysis has focused the search on the more evolved rock types that likely, as today, do not represent the major volume of Earth's crust.

The short-lived $^{146}Sm$-$^{142}Nd$ isotopic system [half life ($T_{1/2}$) = 103 million years (My)] has proven useful for investigating the early differentiation of the silicate portion of Earth. Recent measurements of the $^{146}Sm$-$^{142}Nd$ system in Eoarchean (4.0 to 3.6 Ga) rocks, primarily from Greenland, show excesses in $^{142}Nd/^{144}Nd$ ratios of 10 to 20 parts per million (ppm) compared to modern terrestrial standards testifying to Earth differentiation events within a few tens of million years of Earth formation (*3*–*7*). The high $^{142}Nd/^{144}Nd$ measured for these rocks indicate that the Eoarchean crustal rocks were sourced in a mantle with high Sm/Nd ratio. We describe evidence from the Nuvvuagittuq greenstone belt that a complimentary, low Sm/Nd ratio, reservoir is also found in the terrestrial rock record and that these rocks may be the oldest yet discovered on Earth.

The recent discovery of the Nuvvuagittuq greenstone belt in Ungava, Québec, provides a new suite of Eoarchean rocks with which to further our understanding of the early crust-mantle system. The Nuvvuagittuq belt exposes volcanic and metasedimentary rocks in an isoclinal synform refolded into a more open south-plunging synform (Fig. 1) (*8*) and is surrounded by a 3.66-billion-

[1]Earth and Planetary Sciences Department, McGill University, 3450 University Street, Montreal, Quebec, H3A 2A7, Canada. [2]Department of Terrestrial Magnetism, Carnegie Institution of Washington, 5241 Broad Branch Road, NW, Washington, DC 20015, USA. [3]GEOTOP (Centre de recherche en géochemie et géodynamique), Université du Québec à Montréal, Post Office Box 8888, Succursale Centre-ville, 210, Président-Kennedy Avenue, Montreal, Quebec H3C 3P8, Canada.

*To whom correspondence should be addressed. E-mail: oneil_jo@eps.mcgill.ca